

**Irradiation damage in  $\text{Gd}_2\text{Ti}_2\text{O}_7$  single crystals: Ballistic versus ionization processes**S. Moll,<sup>1,\*</sup> G. Sattonnay,<sup>2</sup> L. Thomé,<sup>1</sup> J. Jagielski,<sup>3</sup> C. Decorse,<sup>4</sup> P. Simon,<sup>5</sup> I. Monnet,<sup>6</sup> and W. J. Weber<sup>7,8</sup><sup>1</sup>*Centre de Spectrométrie Nucléaire et de Spectrométrie de Masse, CNRS-IN2P3-Université Paris Sud, UMR 8609, Bât. 108, F-91405 Orsay, France*<sup>2</sup>*LEMHE/ICMMO, Université Paris Sud, UMR 8182, Bât. 410, F-91405 Orsay, France*<sup>3</sup>*Institute for Electronic Materials Technology, Wolczynska 133, 01-919 Warsaw, Poland and The Andrzej Soltan Institute for Nuclear Studies, 05-400 Swierk/Otwock, Poland*<sup>4</sup>*LPCE/ICMMO, Université Paris Sud, UMR 8182, Bât. 410, F-91405 Orsay, France*<sup>5</sup>*CEMHTI, CNRS, UPR 3079, 1D avenue de la Recherche Scientifique F-45071 Orléans Cedex 2, France*<sup>6</sup>*CIMAP-GANIL, CEA-CNRS-ENSICAEN, BP 5133, F-14070 Caen Cedex 5, France*<sup>7</sup>*Department of Materials Science and Engineering, University of Tennessee, Knoxville, Tennessee 37996, USA*<sup>8</sup>*Materials Science and Technology Division, Oak Ridge National Laboratory, Oak Ridge, Tennessee 37831, USA*

(Received 1 March 2011; revised manuscript received 23 May 2011; published 24 August 2011)

The structural transformations induced in  $\text{Gd}_2\text{Ti}_2\text{O}_7$  single crystals irradiated at high energies (870-MeV Xe), where ionization processes (electronic stopping) dominate, and at low energies (4-MeV Au), where ballistic processes (nuclear stopping) dominate, have been studied via the combination of Rutherford backscattering spectrometry and channeling (RBS/C), Raman spectroscopy, and transmission electron microscopy (TEM) experiments. At high energy, amorphization occurs directly in individual ion tracks from the extreme electronic-energy deposition, and full amorphization results from the overlapping of these tracks as described by a direct impact model. The track diameters lie in the range 6–9 nm. At low energy, amorphization occurs via indirect processes, driven by ballistic nuclear energy deposition from the ions, that is accounted for in the framework of both direct-impact/defect-stimulated and multi-step damage accumulation models. The ion fluence for total amorphization of the irradiated layer is much higher at low energy (0.5 ion  $\text{nm}^{-2}$ ) than at high energy (0.05 ion  $\text{nm}^{-2}$ ), consistent with the nuclear stopping at low energy (5.2 keV/nm) compared to the electronic stopping at high energy (29 keV/nm).

DOI: [10.1103/PhysRevB.84.064115](https://doi.org/10.1103/PhysRevB.84.064115)

PACS number(s): 61.80.-x

**I. INTRODUCTION**

Pyrochlores with the  $\text{A}_2\text{B}_2\text{O}_7$  stoichiometry provide a large array of structural and physical properties related to their various chemical compositions. In particular, due to the capability to incorporate actinides (e.g., U, Np, Th, Pu, Am, and Cm), the  $\text{A}_2^{3+}\text{B}_2^{4+}\text{O}_7$  series is of great interest in the field of nuclear waste management.<sup>1</sup> Among a few hundred synthetic compositions of the pyrochlore structure, titanate-based forms have been the focus of major research endeavors for several decades owing to their presence in devitrified glass waste forms, glass ceramic waste forms, and titanate ceramic waste forms.<sup>2,3</sup> Of these, the titanate-based ceramic host Synroc<sup>4</sup> is best known. Pyrochlore phases within Synroc and glass ceramic waste forms are considered for the immobilization of minor actinides (Np, Am, Cm) from advanced fuel cycles, as well as Pu from dismantled nuclear weapons.<sup>3,5</sup>

The earliest work on radiation damage to pyrochlore was the study of alpha-decay damage in  $^{244}\text{Cm}$ -doped  $\text{Gd}_2\text{Ti}_2\text{O}_7$ , which became amorphous primarily from the ballistic collision cascades produced by  $^{240}\text{Pu}$  alpha-recoil nuclei<sup>6,7</sup>; however, the high spontaneous fission rate of  $^{244}\text{Cm}$  resulted in the formation of readily observable fission tracks whose structure was never resolved. Since that time, the effects of radiation damage in pyrochlores have been largely studied in the energy range from a few keV to a few MeV using ions. In this energy regime ballistic processes are predominant and proportional to the nuclear stopping power  $S_n$ . The elastic collisions cause direct atomic displacements that are responsible for the atomic-scale rearrangement of the structure, similar to the processes occur-

ring due to alpha decay. However, the irradiation response of pyrochlores is narrowly linked to the chemical composition and the structural-phase stability.<sup>3,8</sup> For instance, rare earth titanates ( $\text{RE}_2\text{Ti}_2\text{O}_7$ ) undergo a phase transition toward an amorphous state, whereas rare earth zirconates ( $\text{RE}_2\text{Zr}_2\text{O}_7$ ) are subjected to a pyrochlore to defect-fluorite phase transformation. Moreover, the amorphization resistance increases with increasing Rare Earth (RE) size, indicating the major role played by the A cation.<sup>3,9</sup> Recently, a few studies have been undertaken to understand the behavior of pyrochlores under irradiation with high-energy heavy ions.<sup>10–13</sup> In this energy regime, the high electronic-energy loss,  $S_e$ , from the passage of a swift heavy ion induces the formation of an electrostatically unstable cylinder of ionized atoms and the emission of hot electrons. Latent tracks are created that should be similar to fission tracks, and phase transitions are expected to occur directly within the tracks. In the case of the  $\text{Gd}_2(\text{Ti}_{1-x}\text{Zr}_x)_2\text{O}_7$  composition, the structure of the ion tracks depends on the pyrochlore composition, with the damage cross sections increasing with Ti content.<sup>10</sup> Here again,  $\text{Gd}_2\text{Zr}_2\text{O}_7$  is transformed into an anion-deficient fluorite structure, whereas  $\text{Gd}_2\text{Ti}_2\text{O}_7$  evolves toward an amorphous state. As discussed recently,<sup>14</sup> this difference in radiation response in the high electronic-energy loss regime is due to the effect of order-disorder tendencies on recrystallization behavior.<sup>8</sup>

Although the energy deposition and the irradiation damage processes at low and high energy are clearly different, a similar final damage state is generally observed in these pyrochlore systems independent of whether the damage is produced by

TABLE I. Irradiation parameters.  $R_p$  and  $\Delta R_p$  are the ion-projected ranges and the range stragglings, respectively;  $S_n$  and  $S_e$  are the nuclear and electronic stopping powers, respectively. These data were calculated with the TRIM Monte-Carlo code.<sup>15</sup>

Ion	Energy (MeV)	Fluence (nm <sup>-2</sup> )	$R_p$ ( $\mu\text{m}$ )	$\Delta R_p$ ( $\mu\text{m}$ )	$S_n$ (keV/nm) <sup>a</sup>	$S_e$ (keV/nm) <sup>a</sup>
<sup>124</sup> Xe <sup>20+</sup>	870	10 <sup>-4</sup> –0.1	35.5	3	0.03	29
<sup>196</sup> Au <sup>2+</sup>	4	0.01–1	0.5	0.4	5.2	2

<sup>a</sup>The values for  $S_n$  and  $S_e$  are averaged in the first micrometer for 870-MeV Xe-ion irradiation; they are taken at the maximum of the damage profile ( $\sim 0.4 \mu\text{m}$ ) for 4-MeV Au-ion irradiation.

elastic collisions at low energy or by high electronic-energy deposition at high energy. In the present work, Gd<sub>2</sub>Ti<sub>2</sub>O<sub>7</sub> single crystals are irradiated with high-energy and low-energy heavy ions in order to determine the characteristic damage accumulation processes and understand the underlying reasons for the similarity in damage-end states. In addition, the low-energy irradiation results can be compared to damage-accumulation behavior from alpha-decay in Cm-doped Gd<sub>2</sub>Ti<sub>2</sub>O<sub>7</sub>, and the high-energy irradiation results will provide insights into both the structure and stability of fission tracks in Gd<sub>2</sub>Ti<sub>2</sub>O<sub>7</sub> and their contribution to damage-accumulation processes, which are important for the immobilization of minor actinides, such as <sup>244</sup>Cm, that have a high spontaneous fission rate. The irradiation-induced damage accumulation is investigated by Rutherford backscattering spectrometry (RBS/C), and both Raman spectroscopy and transmission electron microscopy (TEM) are used to characterize the nature of the damage in the final state. Mechanisms for irradiation-induced damage are then discussed to explain similarities and differences in the behavior of solids subjected to nuclear or electronic processes.

## II. EXPERIMENTAL

Gd<sub>2</sub>Ti<sub>2</sub>O<sub>7</sub> single crystals were synthesized at the LEMHE in Orsay from polycrystalline samples of the same composition. The latter were produced from Gd<sub>2</sub>O<sub>3</sub> and TiO<sub>2</sub> oxide powders. Stoichiometric amounts of Gd<sub>2</sub>O<sub>3</sub> and TiO<sub>2</sub> were mixed thoroughly and heated at 1200 °C for 15 h. The resulting mixture was well grounded and isostatically pressed into rods of about 8-cm long and 6-mm diameter. Rods were sintered at 1400 °C in air for 72 h. This procedure was repeated until the Gd<sub>2</sub>Ti<sub>2</sub>O<sub>7</sub> compound was formed, as revealed by x-ray diffraction analysis. From polycrystalline sample rods, single crystals of Gd<sub>2</sub>Ti<sub>2</sub>O<sub>7</sub> were grown by a floating zone method using an infrared-image furnace. X-ray Laue diffraction was employed to orient the single crystals in the (110) direction. Disks with a thickness of 500  $\mu\text{m}$  were then cut from oriented single crystal rods and subsequently polished on diamond disks with the wedge technique to mirror finish. All the samples were finally annealed at 1400 °C for 10 h to remove polishing damage. The lattice parameter is 1.018 nm.

A first series (hereafter labeled HE) of Gd<sub>2</sub>Ti<sub>2</sub>O<sub>7</sub> single crystals were irradiated at room temperature with 870-MeV Xe<sup>20+</sup> ions provided by the GANIL facility in Caen (SME line). The ion fluences ranged from 10<sup>-4</sup> to 0.1 ion nm<sup>-2</sup>. The ion flux was limited to 10<sup>-6</sup> ion nm<sup>-2</sup>s<sup>-1</sup> in order to avoid excessive target heating during irradiation. A second series (hereafter labeled LE) of Gd<sub>2</sub>Ti<sub>2</sub>O<sub>7</sub> single crystals were irradiated at room temperature with 4-MeV Au<sup>2+</sup> ions delivered by the ARAMIS accelerator of the JANNuS facility

located at CSNSM in Orsay. The ion fluences ranged from 0.01 to 1 ion nm<sup>-2</sup>. The ion flux was limited to 10<sup>-3</sup> ion nm<sup>-2</sup>s<sup>-1</sup> in order to avoid excessive target heating during irradiation. Table I summarizes the irradiation conditions as well as the values of the ion-projected range ( $R_p$ ) and of the nuclear ( $S_n$ ) and electronic ( $S_e$ ) stopping powers for both series of irradiations, according to SRIM2008 calculations.<sup>15</sup>

For both series of crystals, RBS/C experiments were performed with a 3-MeV He<sup>2+</sup> beam delivered by the ARAMIS accelerator. A difference is that, for LE crystals, the RBS/C analyses were performed on one sample *in situ* during irradiation at increasing ion fluences, whereas for HE crystals the RBS/C analyses were performed *ex situ* on several samples irradiated at different ion fluences. For RBS/C analyses, a 15-nm-thick carbon layer was deposited on the surface of samples to avoid charging effects. The channeling data were analyzed with the Monte-Carlo McChasy code developed at the Soltan Institute for Nuclear Studies in Warsaw.<sup>16</sup>

Raman characterizations were performed with a Renishaw Invia Reflex device equipped with a Leica DM2500 microscope (100 $\times$  objective). The chosen excitation-laser radiation was the 514.5-nm Ar<sup>+</sup> line, after several tests at 457, 488, 633, and 785 nm. Samples were mounted on a motorized XYZ stage, allowing very accurate displacements (accuracy  $\sim 100$  nm in all directions) and depth scans through confocal filtering. No specific polarization conditions were applied; the natural polarization of the spectrometer strongly favors vertical-vertical (VV) polarization conditions, this means that the excitation and the scattered lights are both vertically polarized, giving access to the diagonal terms of the Raman tensor. In the depth scans for HE samples, the depths were corrected from the optical index effect (depth = vertical displacement under the microscope divided by refraction index). In the case of LE samples, because of inaccurate Raman measurements in the surface region, crystals were cut along the direction normal to the surface, and the Raman measurements were performed along the sample slice.

*Ex situ* TEM observations were carried out with a 200-kV Tecnai G<sup>2</sup>20 microscope. On one hand, for the LE samples, cross-sectional specimens were prepared in order to determine the nature of radiation-induced damage as a function of depth. Crystals were first thinned down by mechanical polishing using the tripod technique to around 20  $\mu\text{m}$  and then by Ar-ion milling using a Gatan 691 ion polishing system (PIPS) to electron transparency. On the other hand, for HE sample, plan-view specimens were prepared in order to determine the track core structure and the track radii. Crystals were thinned down by mechanical polishing to electron transparency. Finally, a

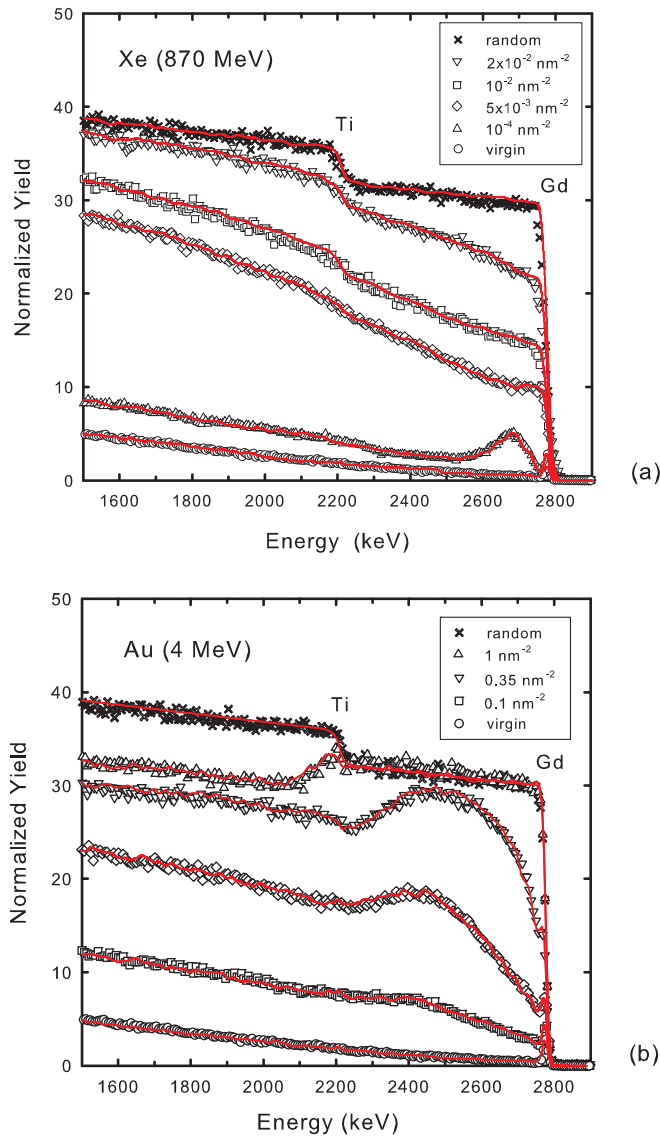


FIG. 1. (Color online) RBS spectra (Gd and Ti signals) recorded on  $\text{Gd}_2\text{Ti}_2\text{O}_7$  single crystals irradiated with (a) 870-MeV Xe or (b) 4-MeV Au ions in random (crosses) and  $\langle 110 \rangle$ -aligned (other symbols) directions. Energy of analyzing He beam: 3 MeV. Solid lines are fits to experimental data with the McChasy code.<sup>16</sup>

carbon grid was placed on the TEM sample holder to evacuate charges on the specimen surface.

### III. RESULTS

#### A. Damage accumulation

Figure 1 displays RBS spectra recorded on  $\text{Gd}_2\text{Ti}_2\text{O}_7$  single crystals irradiated with 870-MeV Xe (HE series) and 4-MeV Au (LE series) ions. The random spectra registered for the two series [crosses in Figs. 1(a) and 1(b)] exhibit a major contribution of the Gd sublattice below 2800 keV and a smaller contribution of the Ti sublattice below 2200 keV (the part of spectra corresponding to the O lattice is not shown on the figure). The RBS spectra recorded along the  $\langle 110 \rangle$  crystallographic orientation on virgin single crystals present a low value of the normalized yield below the surface peak

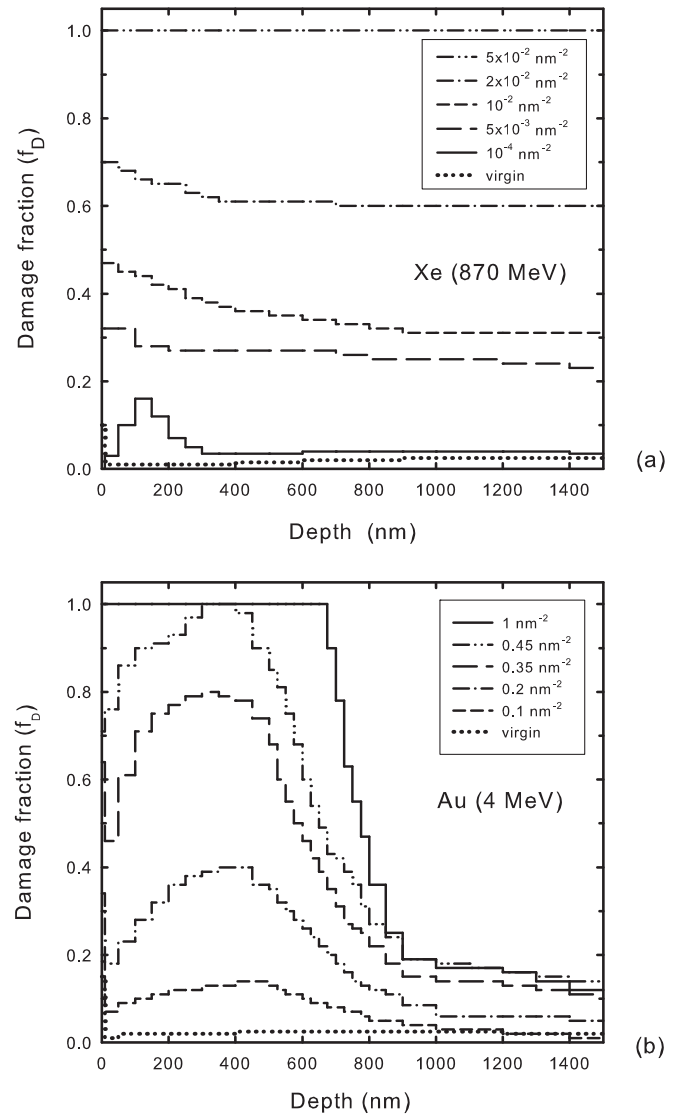


FIG. 2. Damage fraction ( $f_D$ ) as a function of the depth extracted from the fits to experimental RBS data for  $\text{Gd}_2\text{Ti}_2\text{O}_7$  single crystals irradiated with (a) 870-MeV Xe or (b) 4-MeV Au ions at the indicated fluences.

corresponding to the Gd sublattice ( $\chi_{\min} \sim 0.03$ ), which attests to the good quality of samples. The  $\langle 110 \rangle$  aligned spectra registered on the HE series [Fig. 1(a)] present a constant dechanneling in the entire analyzed region. This dechanneling increases with increasing ion fluence, and the aligned yield reaches the random level at  $0.05 \text{ ion nm}^{-2}$  (not shown on the figure). The  $\langle 110 \rangle$  aligned spectra registered on the LE series [Fig. 1(b)] exhibit a bump around 2500 keV with an amplitude that increases with increasing ion fluence. At  $0.4 \text{ ion nm}^{-2}$  (not shown on the figure), the aligned spectrum reaches the random level at 2500 keV, indicating a state of total disorder at this depth. At higher fluences, the totally disordered region extends toward both lower and greater depths and reaches the sample surface at  $1 \text{ ion nm}^{-2}$ .

Damage-depth distributions may be extracted from the analysis of channeling spectra by using the McChasy code.<sup>16</sup> The main assumption used for fitting the data is that a given fraction of target atoms (hereafter referred to as damage fraction) is

randomly displaced from original lattice sites. Moreover, since the backscattering cross section depends on the square of the atomic number of an element, the Gd signal is predominant in this analysis, so we have assumed a similar disorder on all sublattices. Figure 2 shows the results obtained for both series of crystals. Figure 2(a) exhibits a rather constant level of disorder in the whole analyzed depth, which increases with increasing ion fluence [except at very low fluence ( $10^{-4}$  ion  $\text{nm}^{-2}$ ) where only the near-surface region is disordered]. Total disorder ( $f_D = 1$ ) is reached at  $5 \times 10^{-2}$  ion  $\text{nm}^{-2}$ . Figure 2(b) shows very different disorder profiles that exhibit a progressive increase of  $f_D$  with increasing ion fluence at a depth around 400 nm, which reaches unity (total disorder) at 0.45 ion  $\text{nm}^{-2}$ ; with further increases in fluence to 1 ion  $\text{nm}^{-2}$ , the disordered layer spreads from the sample surface to a depth of  $\sim 700$  nm.

The irradiation-damage accumulation behavior is well described by the increase in damage fraction ( $f_D$ ) as a function of ion fluence, shown in Fig. 3, for both irradiation series. For the HE series  $f_D$  was taken around 500 nm to avoid surface effects; whereas for the LE series,  $f_D$  was taken at the depth of maximum damage production (around 400 nm). Figure 3 shows that the biggest difference in the damage accumulation behavior between HE and LE experiments lies in the fact that saturation ( $f_D = 1$ ) occurs at a fluence one order of magnitude higher ( $\sim 0.5$  ion  $\text{nm}^{-2}$ ) for LE ions than for HE ions ( $\sim 0.05$  ion  $\text{nm}^{-2}$ ). These results are interpreted within the framework of phenomenological models presented in the next section.

### B. Characterization of radiation damage

The characterization of the damage induced by irradiation in  $\text{Gd}_2\text{Ti}_2\text{O}_7$  single crystals was performed by using Raman spectrometry and TEM observations. Figure 4(a) shows Raman spectra recorded on the LE sample irradiated to the highest ion fluence used (1 ion  $\text{nm}^{-2}$ ). Six active modes are observed. After irradiation the intensity of the sharp peaks significantly decreases, indicating a distortion of the chemical bonds and a local disordering, and a new broad band appears around  $750 \text{ cm}^{-1}$  that is associated with the formation of an amorphous phase.<sup>17</sup> Similar spectra are obtained for HE samples but are not shown here (see data obtained on polycrystalline  $\text{Gd}_2\text{Ti}_2\text{O}_7$  samples in Ref. 13).

Figure 4(b) displays Raman mapping recorded on the LE sample irradiated to the highest ion fluence (1 ion  $\text{nm}^{-2}$ ), which represents the depth distribution of Raman-band intensities. The step between two points is 100 nm. The amorphous band is observed from the sample surface up to a depth of  $\sim 500$  nm, which fits reasonably well the nuclear energy loss represented in Fig. 4(c). Moreover, the depth over which the amorphous signal is observed in this Raman mapping is close to the totally disordered region measured by RBS/C on the same crystal [Fig. 2(b)]. It is worth mentioning that previous Raman measurements performed on  $\text{Gd}_2\text{Ti}_2\text{O}_7$  irradiated with LE ions did not show any modifications in the Raman signal arising from the irradiated layer, certainly due to an insufficient depth resolution to probe this shallow layer.<sup>18</sup> In the present work, due to the special preparation of cross-sectional samples, the depth resolution was sufficiently high to analyze the damaged depth and to obtain reliable

Raman-depth mapping for a material irradiated at LE. A similar map is obtained for the HE sample irradiated to the highest fluence (0.1 ion  $\text{nm}^{-2}$ ), where the depth profile of the amorphized layer fits well the electronic-energy loss (see similar data obtained on polycrystalline  $\text{Gd}_2\text{Ti}_2\text{O}_7$  samples in Ref. 13).

Figure 5 presents TEM micrographs (plane views) recorded on a crystal irradiated at HE to a small fluence of  $2 \times 10^{-3}$  ion  $\text{nm}^{-2}$  that clearly show the presence of tracks formed in the wake of swift ions. Figure 5(a) (recorded at the lowest magnification) indicates that the number of ion tracks is consistent with the irradiation fluence. Figure 5(b) (recorded at the highest magnification) shows that these tracks exhibit two main regions: (i) the core, with a diameter of 6–7 nm, that is totally amorphous; and (ii) a smaller outer shell that contains a strongly disordered structure. In contrast, micrographs recorded on specimens irradiated at LE to low fluences do not exhibit ion tracks. Since swift heavy ions have negligible nuclear energy loss at these shallow depths, this difference in behavior demonstrates that the formation of tracks in  $\text{Gd}_2\text{Ti}_2\text{O}_7$  is due to the high electronic-energy deposition from swift heavy ions. Cross-sectional TEM micrographs for a crystal irradiated at LE to a final fluence of 1 ion  $\text{nm}^{-2}$  are shown in Figs. 6(a) and 6(b) for different magnifications. They exhibit three regions of damage: (1) an amorphous layer (see the diffraction pattern in the inset) extending from the surface of the specimen to a depth of  $\sim 800$  nm; (2) a narrow layer below the amorphous region that contains small defect clusters with a size on the order of 1 nm; and (3) a virgin zone at greater depth not affected by the ion beam. The presence of small defect clusters at the end of the ion trajectory [Fig. 6(b)], instead of latent tracks as in the case of high-energy ion irradiations [Fig. 5(b)], confirms that the mechanisms of defect formation are dependent on the ion energy loss process.

## IV. DISCUSSION

Several phenomenological models have been developed to account for damage accumulation in ion-irradiated solids. In the case of high-energy irradiations, the model proposed by Gibbons in the early 1970s<sup>19</sup> provides a reasonable description of the experimental damage accumulation when the number  $n$  of ion impacts needed to produce the final damage state is equal to 1. This feature is due to the fact that, in the energy range above  $\sim 1 \text{ MeV/u}$ , each incoming ion creates a permanent track [see a schematic representation in Fig. 7(a)], clearly evidenced in Fig. 5, and the overall damage results from the accumulation and overlapping of individual tracks. Thus, the damage fraction ( $f_D$ ) can be accounted for in the framework of a single-impact mechanism according to the reduced Gibbons model ( $n = 1$ )<sup>19</sup>:

$$f_D = f_D^{\text{sat}} [1 - \exp(-\sigma \Phi)] \quad (1)$$

where  $f_D^{\text{sat}}$  is the damage fraction at saturation (i.e., at very high fluences), which is equal to 1 in case of amorphization,  $\sigma$  is the damage cross section (linked to the diameter of ion tracks, see following discussion), and  $\Phi$  is the irradiation-ion fluence.

The situation becomes far more complicated in the case of low-energy irradiations where no ion tracks are formed

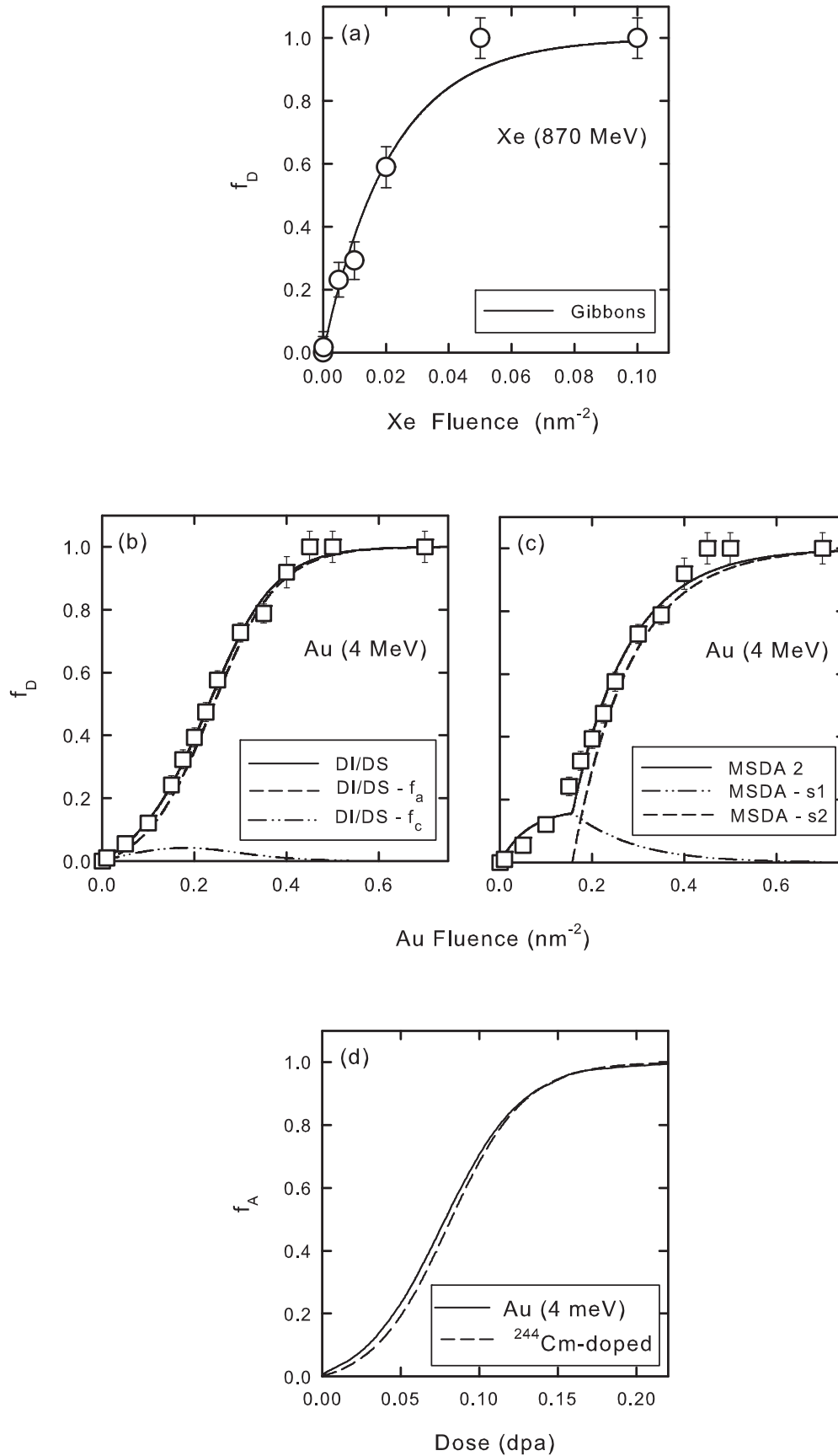


FIG. 3. Amorphization build-up of  $Gd_2Ti_2O_7$  single crystals irradiated with (a) 870-MeV Xe or (b), (c) 4-MeV Au ions, or arising from (d)  $^{244}Cm$  decay.<sup>33</sup> Solid lines are fits to experimental data with Eqs. (1)–(4) derived from the (a) Gibbons,<sup>18</sup> (b) DI/DS,<sup>20,21</sup> and (c) MSDA<sup>22,23</sup> models. Dashed and dotted-dashed lines (b), (c) represent the different contributions defined in Eqs. (2)–(4) for the DI/DS and MSDA models.

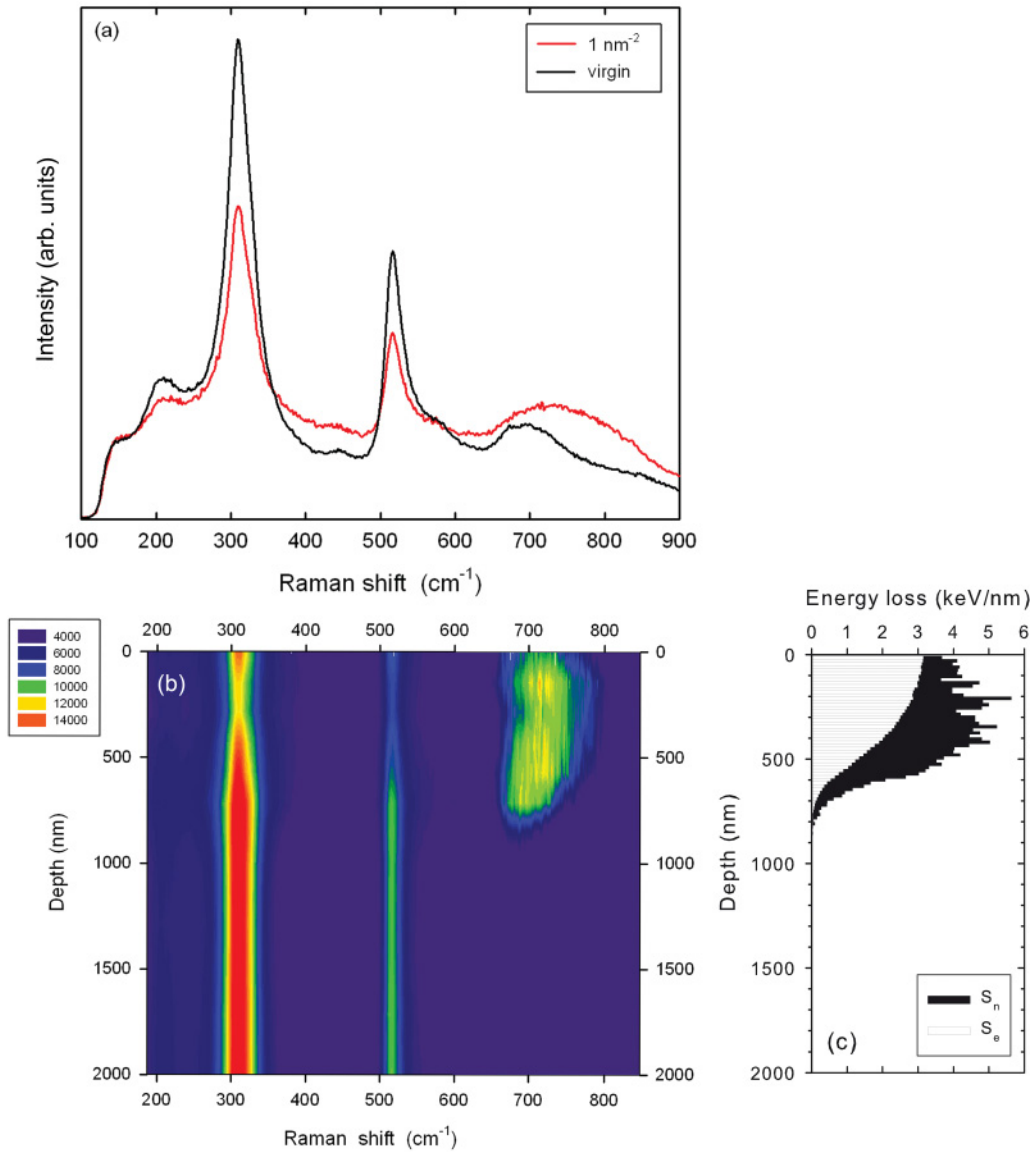


FIG. 4. (Color online) (a) Raman spectra recorded on Gd<sub>2</sub>Ti<sub>2</sub>O<sub>7</sub> single crystals before (black line) and after (red line) irradiation with 4-MeV Au ions at 1 ion nm<sup>-2</sup>. (b) Raman-line map on a Gd<sub>2</sub>Ti<sub>2</sub>O<sub>7</sub> single crystal irradiated with 4-MeV Au ions at 1 ion nm<sup>-2</sup>. The color scale is blue–green–yellow–red by increasing order of intensity. In a gray scale, the amorphous component (between 650 and 800 cm<sup>-1</sup> and from the surface up to a depth of 700 nm) appears lighter. (c) Variation of S<sub>c</sub> and S<sub>n</sub> with depth for Gd<sub>2</sub>Ti<sub>2</sub>O<sub>7</sub> irradiated with 4-MeV Au ions.

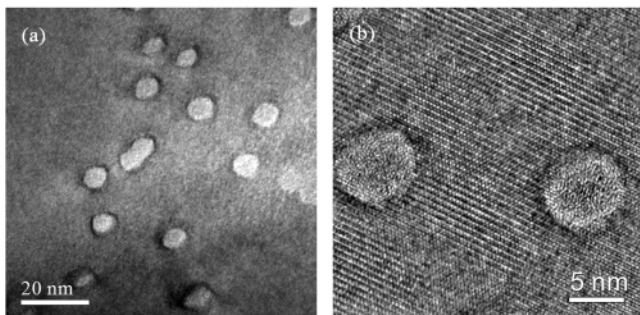


FIG. 5. High-resolution TEM micrographs with different magnifications recorded on a Gd<sub>2</sub>Ti<sub>2</sub>O<sub>7</sub> sample irradiated with 870-MeV Xe ions at 2 × 10<sup>-3</sup> ion nm<sup>-2</sup> showing ion tracks (from a work performed by J. Zhang and M. Lang).

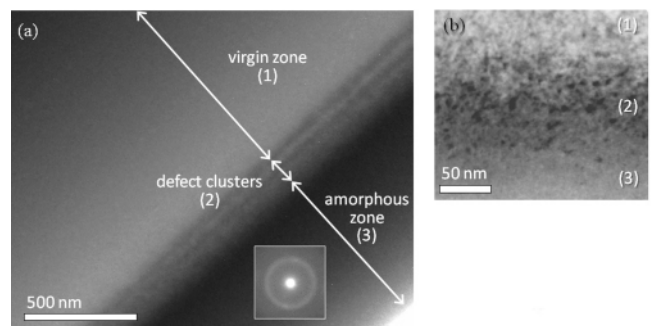


FIG. 6. TEM micrographs recorded on a Gd<sub>2</sub>Ti<sub>2</sub>O<sub>7</sub> sample irradiated with 4-MeV Au ions at 1 ion nm<sup>-2</sup> representing (i) an overall view of the different damaged layers as a function of depth, and (ii) an enlargement of the defect cluster region.

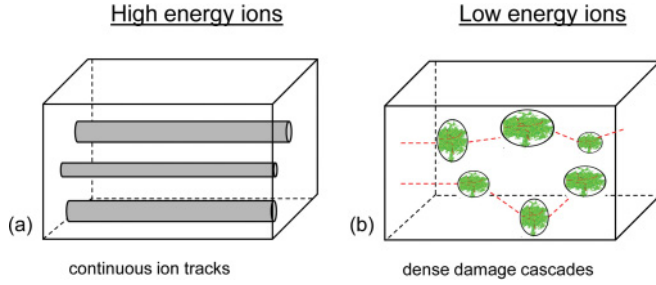


FIG. 7. (Color online) Schematic representation of the damage formation in Gd<sub>2</sub>Ti<sub>2</sub>O<sub>7</sub> crystals irradiated with (a) high or (b) low energy ions.

but where the damage results from the creation of isolated defect cascades [as illustrated in Fig. 7(b)]. Very different damage accumulation mechanisms, varying from more or less complicated sigmoidal dependences up to multistep processes, including stages characterized by a decrease of the damage level, have been reported in the literature.<sup>20</sup> The direct-impact/defect-stimulated (DI/DS)<sup>21,22</sup> and the multi-step damage accumulation (MSDA)<sup>23,24</sup> models have been shown to provide accurate descriptions for the damage accumulation in different materials irradiated with ions in the energy range below  $\sim 10$  keV/u. It is worth mentioning that a model based on the assumption that ion-beam amorphization results from the nucleation and growth of amorphous islands (or clusters)<sup>25</sup> can also fit the RBS/C data obtained in this study. Nevertheless, such a single-parameter model does not describe the atomic-level details of irradiation-induced amorphization processes occurring in crystals from the complex damage mechanisms involved in particle-solid interactions, where competition coexists between the growth of amorphous clusters induced by a direct-impact mechanism, defect-stimulated amorphization, and the formation and interaction of defects in the crystalline structure.

The DI/DS model assumes that the accumulated damage ( $f_D$ ) results from amorphous and damaged-crystalline regions according to the relationship:  $f_D = f_A + f_C$ , where  $f_A$  is the amorphous fraction and  $f_C$  is the damaged fraction due to irradiation-induced point defects and small defect clusters in the remaining crystalline regions. In this framework  $f_A$  may be written<sup>21</sup>

$$f_A = 1 - (\sigma_A + \sigma_S) / \{\sigma_S + \sigma_A \exp(\sigma_A + \sigma_S)\Phi\}, \quad (2)$$

where  $\sigma_A$  and  $\sigma_S$  are the cross sections for direct and defect-stimulated amorphization, and  $\Phi$  is the irradiation fluence. The damage fraction related to the presence of defects in the crystalline structure ( $f_C$ ) is usually reproduced by a simple defect accumulation model<sup>22</sup>:

$$f_C = f_C^{\text{sat}} [1 - \exp(-\sigma_C \Phi)] (1 - f_A) \quad (3)$$

where  $f_C^{\text{sat}}$  is the saturation value for the defect-induced disorder, and  $\sigma_C$  is the corresponding cross section, which includes the probability for defect-recombination processes.

The MSDA model is based on the assumption that the production of damage results from a series of successive atomic rearrangements (called steps) triggered by either microscopic or macroscopic mechanisms. This model assumes that, when the volume of collision cascades is too small (as it is the case for

LE irradiations), the formation of a permanent defect structure requires the destabilization of a sufficiently large volume of the irradiated material. Thus, once a structure becomes unstable, due to, e.g., the formation of stresses, each ion impact leads to the transformation of a given volume of the crystal into a new metastable atomic configuration that is far from equilibrium. Such a process is controlled by the probability that each ion hits an unmodified volume of the material, so that it can be described within the framework of a direct-impact mechanism. The successive defect transformations lead to changes in the damage accumulation build-up that is thus composed of several steps, each step being related to a given type of dominant defect configuration. According to the previous hypotheses, the equation which accounts for the multistep transformation process may be written as<sup>23,24</sup>

$$f_D = \sum_{i=1}^{n-1} \left\{ f_{D,i}^{\text{sat}} G[1 - \exp(-\sigma_i(\Phi - \Phi_i))] \right. \\ \times \left. \prod_{k=i+1}^n [\exp(-\sigma_{k+1}(\Phi - \Phi_{k+1}))] \right\} \\ + f_{D,n}^{\text{sat}} G[1 - \exp(-\sigma_n(\Phi - \Phi_n))], \quad (4)$$

where  $n$  is the number of steps required for the achievement of the total process,  $f_{D,i}^{\text{sat}}$  is the level of damage at saturation,  $\sigma_i$  is the cross section for damage formation, and  $\Phi_i$  is the threshold irradiation fluence for the  $i^{\text{th}}$  step.  $G$  is a function which is zero when its argument is negative or identical to the argument if the latter is positive. In fact,  $G$  corresponds to a Heaviside function  $H$  multiplied by its argument; here we prefer to use  $G$  instead of  $H$  as it leads to a much simpler form of Eq. (4).

It should be pointed out that DI/DS and MSDA models converge toward the simplified Gibbons Eq. (1) when a single mechanism leads to the formation of permanent damage in a crystal (via, e.g., a direct amorphization process), as was found for high-energy irradiations. Thus, in this case  $\sigma_S = \sigma_C = 0$  for DI/DS and  $n = 1$  for MSDA, so that Eqs. (2) and (4) become identical to Eq. (1).

Figure 3 shows that RBS/C data recorded on HE crystals (a) can be correctly reproduced by using a single-impact description (1), whereas data obtained on LE crystals are well fitted using the (b) DI/DS or (c) MSDA models Eqs. (2)–(4). It is worth noting that more data in the intermediate fluence range are needed to convincingly reproduce the step around  $0.15 \text{ nm}^2$  inherent to the MSDA representation, since this step is much less visible than in the case of other irradiated materials.<sup>20</sup> Actually, two types of atomic rearrangements (defects in the crystalline structure and amorphous domains) were introduced in the models, since previous results showed that they are produced during RT irradiation of Gd<sub>2</sub>Ti<sub>2</sub>O<sub>7</sub>.<sup>3,8</sup> Figures 3(b) and 3(c) also show the different contributions to the total disorder arising from both DI/DS and MSDA models. Table II provides the values of the parameters obtained from the different model fits to the data in Fig. 3. This table shows that very different values for the parameters are obtained from the HE- and LE-irradiation data, and, in the case of LE data, the use of different damage accumulation descriptions allows

TABLE II. Parameters extracted from the fits to RBS/C experimental data with the various models used in this work.

870-MeV Xe	4-MeV Au	
Direct Ion Impact Eq. (1)	DI/DS Eqs. (2), (3)	MSDA Eq. (4)
$n = 1$	$\sigma_A = 0.50 \pm 0.25 \text{ nm}^2$	$n = 2$
$f_D^{\text{sat}} = 1$	$\sigma_S = 13 \pm 2 \text{ nm}^2$	$f_{D,1}^{\text{sat}} = 0.17 \pm 0.10$
$\sigma_1 = 46 \pm 7 \text{ nm}^2$	$f_C^{\text{sat}} = 0.15 \pm 0.4$	$\sigma_1 = 16 \pm 10 \text{ nm}^2$
	$\sigma_C = 2.8 \pm 4.0 \text{ nm}^2$	$\Phi_2 = 0.16 \pm 0.02 \text{ ion nm}^{-2}$
		$f_{D,2}^{\text{sat}} = 1$
		$\sigma_2 = 8.1 \pm 1.4 \text{ nm}^2$

one to compare the parameters extracted from the DI/DS and MSDA models.

The Raman data obtained on HE crystals demonstrate that amorphization is due to the large electronic-energy loss deposited by swift heavy ions, since the thickness of the amorphized layer is perfectly consistent with the ion electronic-energy loss. According to the schematic representation of Fig. 7(a), the amorphization results from the formation and overlapping (at high fluences) of the ion tracks shown in the TEM micrographs of Fig. 5. In this illustration, the amorphization cross section ( $\sigma_1$ ) obtained from the fit to RBS/C data provides an indirect value of the track diameter ( $d$ ), according to the equation:

$$d = 2(\sigma_1/\pi)^{1/2}. \quad (5)$$

Table III summarizes the values of  $\sigma_1$  and  $d$  obtained in this work (using RBS/C, TEM, and Raman) and previously reported in Ref. 13 for  $\text{Gd}_2\text{Ti}_2\text{O}_7$  polycrystals. For single crystals the value of track diameters obtained indirectly by fitting RBS/C and Raman data or directly on TEM micrographs are very close (they are also very close to the diameter of fission tracks observed in Cm-doped  $\text{Gd}_2\text{Ti}_2\text{O}_7$ ). These consistent results provide strong evidence that the representation presented previously is realistic. Table III also shows that total track diameters (i.e., amorphous core plus outer disordered shell) determined for single- and polycrystals by the same characterization methods (Raman and TEM) agree well within the limit of experimental uncertainties. In fact, as mentioned in Ref. 13, since tracks are more or less discontinuous, their diameter varies with depth, so that the observation of HRTEM plane views may lead to uncertainties in the determination of track diameters. Moreover, RBS/C gives lower values of track

diameter, owing to the fact that this technique is more sensitive to amorphous regions than to disordered halos.

Figure 7(b) shows a schematic representation of the damage induced by LE ions where nuclear collisions lead to the formation of damage cascades. The Raman map and the TEM micrographs of Figs. 4 and 6 confirm this representation, since the amorphized layer is consistent with the ion nuclear energy loss. By analogy with irradiations involving HE ions slowing down by electronic-energy loss, where the damage cross section ( $\sigma_1$ ) is simply the cross section of the melt cylinder around the ion trajectories (tracks), these parameters at low energy may be regarded as the effective cross section of the volume in which the material is affected by the impact of one incident ion (via damage cascades). Thus, Table II indicates that the volume damaged during step 1 by a single ion in the case of 4-MeV Au irradiation ( $\sigma_1 = 16 \text{ nm}^2$  with a rather large uncertainty) is rather close to the volume amorphized during step 2 by a subsequent ion impact ( $\sigma_2 = 8 \text{ nm}^2$ ), these values being much lower than that found for HE irradiation ( $\sigma_1 = 46 \text{ nm}^2$ ). These results are reasonable since the effective volume of displacement cascades should be rather independent of the irradiation fluence: ions incoming at the beginning or at the end of the irradiation process should displace a similar number of atoms from their lattice positions. On the other hand, the volume transformed by a single HE ion is obviously much larger than the total volume of the subcascades created by a LE ion. The threshold fluence for the destabilization of the crystalline structure is low ( $\Phi_2 = 0.16 \text{ ion nm}^{-2}$ ). This latter parameter could be regarded as a measure of the radiation stability of a crystal: the lower the value of  $\Phi_2$ , the higher the susceptibility of the material to amorphization.

TABLE III. Parameters extracted from the fits to damage accumulation build-ups, obtained using RBS/C, Raman, TEM, and XRD (x-ray diffraction) techniques, for  $\text{Gd}_2\text{Ti}_2\text{O}_7$  single- (this work) and polycrystals<sup>13</sup> irradiated with 870-MeV Xe ions.  $\sigma_1$  is the disordering cross section and  $d$  is the track diameter.

	Technique	$\sigma_1$ (nm <sup>2</sup> )	$d$ (nm)
Single crystals	RBS/C	$46.0 \pm 7.0$	$7.6 \pm 0.6$
	TEM <sup>b</sup>	-	$d_A = 6.5 \pm 0.5$ $d_T = 8.7 \pm 0.7$
	Raman	$40.0 \pm 5.0$	$7.1 \pm 0.6$
Polycrystals <sup>a</sup>	XRD	$84.0 \pm 7.0$	$10.3 \pm 0.4$
	TEM	-	$9.6 \pm 0.3$
	Raman	$54.4 \pm 5.5$	$8.3 \pm 0.9$

<sup>a</sup>Ref. 13.

<sup>b</sup> $d_A$  is the track diameter corresponding to the amorphous core, and  $d_T$  is the total track diameter (amorphous core + disordered outer shell).

In the framework of the DI/DS model,  $\sigma_S$  ( $13 \text{ nm}^2$ ) is significantly larger than  $\sigma_A$  ( $0.5 \text{ nm}^2$ ); this latter parameter is generally much smaller than  $\sigma_S$ , as reported in previous studies of other materials.<sup>22,26–29</sup> This result indicates that for LE ions: (i) the probability of direct amorphization is low, consistent with Molecular Dynamics (MD) simulations of cascades in  $\text{Gd}_2\text{Ti}_2\text{O}_7$ ,<sup>30</sup> as well as in other materials,<sup>31,32</sup> and (ii) defect-stimulated amorphization is the dominant mechanism for the damage accumulation in this and other titanate pyrochlores, which is consistent with the complexity of cation interstitial defects in titanate pyrochlores<sup>33</sup> and the decreased mobility of oxygen vacancies with increasing cation disorder.<sup>34</sup> Thus, only a small ion fluence (less than  $0.5 \text{ ion nm}^{-2}$ ) is required to achieve full amorphization. At low fluences, the damage mechanism is dominated by the formation of defective regions represented by  $f_C$ . In the present study, the contribution of cation (primarily Gd) defects to this measured crystalline component is small due to the strong relaxation of cation interstitials into cation antisites,<sup>30</sup> which are not readily observable by RBS/C. Thus, defect-stimulated amorphization is the dominant contribution to the cation disordering process observed. In spite of this result, the defective crystalline component is the key parameter to explain the defect-induced stimulation effect assumed in the DI/DS model and is included in the present work to correctly describe the radiation damage mechanisms. Moreover, it has previously been demonstrated, in the case of pyrochlores with close compositions (e.g.,  $\text{Sm}_2\text{Ti}_2\text{O}_7$ ,  $\text{Ho}_2\text{Ti}_2\text{O}_7$ ), that the defective crystalline component contributes to the total disorder measured on both cation and oxygen sublattices, as well as to the fully described complex radiation-amorphization mechanisms.<sup>27</sup> Furthermore, it should be noted that large uncertainties were obtained for the values of  $f_C$  and  $\sigma_C$  (see Table II). This result can be due to the fact that the number of data is too small in the fluence range ( $0.1$ – $0.2 \text{ ion nm}^{-2}$ ) where the  $f_C$  contribution is significant. This result could also arise from the use of the RBS technique, which averages the signals coming from amorphous and defective regions. Additional measurements of peak intensities in x-ray diffraction experiments may provide an additional approach to quantify the volume fraction of defective but still crystalline material independently and more accurately.

It is interesting to compare the amorphization behavior of  $\text{Gd}_2\text{Ti}_2\text{O}_7$  subjected to 4-MeV Au ion irradiation with that due to self-radiation damage from  $^{244}\text{Cm}$  decay<sup>35</sup> where the relative damage rate is six orders of magnitude lower than in the present study. In order to make this comparison, the local dose in displacements per atom (dpa) is determined at the damage peak for each Au-ion fluence in this study using the SRIM code and threshold displacement energies of 50 eV for Gd, Ti, and O atoms, as was done previously for  $^{244}\text{Cm}$  pyrochlore.<sup>35</sup> The increases in amorphous fraction as a function of dose for these two different irradiation conditions are in excellent agreement, as shown in Fig. 3(d). The agreement is due in part to the similar value of the nuclear stopping power at the damage peak for Au ions ( $5.8 \text{ keV/nm}$ ) and that of the  $96 \text{ keV } ^{240}\text{Pu}$  recoil nucleus in Cm-doped  $\text{Gd}_2\text{Ti}_2\text{O}_7$  ( $5.5 \text{ keV/nm}$ ); furthermore, the high critical temperature for amorphization in

$\text{Gd}_2\text{Ti}_2\text{O}_7$  under ion irradiation,  $980 \text{ K}$ ,<sup>35</sup> supports a dose-rate independence for damage accumulation under these ambient irradiation conditions, as validated previously for several oxide structures.<sup>35</sup> These results further demonstrate that, within the framework of the DI/DS model,  $\sigma_A$  and  $\sigma_S$  (in units of  $\text{dpa}^{-1}$ ) are similar for Au-ion irradiation and alpha-decay damage. This similarity in behavior, despite six orders of magnitude differences in dose rates, validates the use of Au irradiation to simulate alpha-decay damage in pyrochlores and other materials.

The main conclusion arising from the comparison of the analyses made by using DI/DS and MSDA models at LE is that both models yield a reasonable fit of experimental data, thus supporting the assumption of two types of defect configurations to occur during the damage production process. This representation leads to introduce  $n = 2$  in MSDA or both  $f_A$  and  $f_C$  components in DI/DS. It is interesting to note that, despite some differences in the descriptions used, the values of parameters extracted from both models point to similar evolution of damage accumulation. For instance, the saturation levels of the damage due to the presence of defects in the crystalline structure are found to be very close:  $f_C^{\text{sat}} = 0.15 \pm 0.4$  in DI/DS and  $f_{D,1}^{\text{sat}} = 0.17 \pm 0.10$  in MSDA. The most significant difference between the two models is that in DI/DS the amorphous phase is assumed to be formed from the very beginning of the irradiation process, whereas in MSDA amorphization starts above a (small) fluence threshold. The data provided in this work are unable to discriminate this dilemma.

## V. CONCLUSION

The aim of this work was to compare the structural transformations induced in  $\text{Gd}_2\text{Ti}_2\text{O}_7$  single crystals irradiated with high- and low-energy heavy ions (870-MeV Xe and 4-MeV Au). Information on the disorder accumulation, the nature of the radiation defects, and the mechanisms involved in the structural transformations were obtained via the combination of the RBS/C, Raman, and TEM techniques.

At high energy, the large electronic-energy loss within the wake of incoming ions creates individual amorphous tracks at low ion fluences. The overlapping of these ion tracks at high fluences (i.e., above  $0.05 \text{ ion nm}^{-2}$ ) leads to total amorphization of the irradiated layer over a thickness comparable to the electronic-energy deposition calculated with the SRIM code. The amorphization process is well described within the framework of a model based on the direct ion-impact process. The track diameter indirectly determined by a fit of the direct impact model to the RBS/C data ( $7.6 \text{ nm}$ ) is similar to that directly measured on TEM micrographs ( $6$ – $7 \text{ nm}$ ).

Two models (DI/DS and MSDA) were used to describe the damage accumulation from low-energy ion irradiation. In this energy range total amorphization of the irradiated layer occurs at a fluence ( $0.5 \text{ ion nm}^{-2}$ ), which is much higher than that required in the case of high-energy ion irradiation, over a thickness comparable to the nuclear energy deposition calculated with the SRIM code. Contrarily to the results obtained at high energy, no ion tracks are observed, and amorphization does not occur via a single-step process. In

the framework of the DI/DS model, the amorphous phase starts to form at the beginning of irradiation by direct and defect-assisted processes with very different cross sections. In the framework of the MSDA representation, the damage accumulation occurs in two distinct steps, and amorphization is initiated at a fluence threshold that is on the order of  $0.16 \text{ ion nm}^{-2}$ . This discrepancy is related to an essential question about the structural transformations occurring in ion-irradiated materials: is it possible to imagine that very small volumes of crystal can be transformed into a new structure which would be different from the matrix material? Continuous models, such as DI/DS, give a positive answer to this question. Conversely, the MSDA model is based on the assumption of discontinuity: the structure of very small damaged regions is determined by the overall stability of the surrounding matrix, and the type of defects formed may vary depending on macroscopic considerations, as formation of stresses or stoichiometry of the layer. This topic undoubtedly deserves further investigation.

The increases in amorphous fraction as a function of dose for  $\text{Gd}_2\text{Ti}_2\text{O}_7$  subjected to 4-MeV Au ion irradiation or to  $^{244}\text{Cm}$  decay exhibit strong concordance. This similarity in behavior, despite six orders of magnitude differences in dose rates, validates the use of heavy ion irradiation to simulate alpha decay damage in nuclear materials.

#### ACKNOWLEDGMENTS

This work was partially supported by the “Groupement National de Recherche” (GNR) MATINEX, the French-Polish cooperation program n°01-104, the French National Agency for Research Grant RAMIRIS n°ANR 07-BLAN-0282-01, and as part of the Materials Science of Actinides EFRC, an Energy Frontier Research Center funded by the US Department of Energy, Office of Basic Energy Sciences. We would like to acknowledge the staff of the ARAMIS accelerator for their kind assistance during Au-ion irradiation and RBS/C analyses.

---

\*Present address: Pacific Northwest National Laboratory, P.O. Box 999, MS K8-87, Richland, WA 99352, United States. sandmoll@hotmail.com

<sup>1</sup>W. J. Weber, A. Navrotsky, S. Stefanovsky, E. R. Vance, and E. Vernaz, *MRS Bull.* **34**, 46 (2009).

<sup>2</sup>G. Lumpkin, *J. Nucl. Mater.* **289**, 136 (2001).

<sup>3</sup>R. C. Ewing, W. J. Weber, and J. Lian, *J. Appl. Phys.* **95**, 5949 (2004).

<sup>4</sup>A. E. Ringwood, S. E. Kesson, N. G. Ware, W. Hibberson, and A. Major, *Nature (London)* **278**, 219 (1979).

<sup>5</sup>R. C. Ewing and W. J. Weber, in *The Chemistry of the Actinides and Transactinide Elements*, edited by N. M. Edelstein, J. Fuger, and L. R. Morss, (Springer, New York, 2010), Vol. 6, Chap. 35, pp. 3813–3888.

<sup>6</sup>W. J. Weber, J. W. Wald, and H. J. Matzke, *Mater. Lett.* **3**, 4, 173 (1985).

<sup>7</sup>W. J. Weber, J. W. Wald, and H. J. Matzke, *J. Nucl. Mater.* **138**, 196 (1986).

<sup>8</sup>K. E. Sickafus, L. Minervini, R. W. Grimes, J. A. Valdez, M. Ishimaru, F. Li, K. J. McClellan, and T. Hartmann, *Science* **289**, 748 (2000).

<sup>9</sup>G. Sattonnay, S. Moll, L. Thomé, C. Legros, M. Herbst-Ghysel, F. Garrido, J. M. Costantini, and C. Trautmann, *Nucl. Instr. Meth. B* **266**, 3043 (2008).

<sup>10</sup>M. Lang, J. Lian, J. Zhang, F. Zhang, W. J. Weber, C. Trautmann, and R. C. Ewing, *Phys. Rev. B* **79**, 224105 (2009).

<sup>11</sup>M. Patel, V. Vijayakumar, D. K. Avasthi, J. C. Pivin, V. Grover, B. P. Mandal, and A. K. Tyagi, *Nucl. Instr. Meth. B* **266**, 2898 (2008).

<sup>12</sup>S. Moll, G. Sattonnay, L. Thomé, J. Jagielski, C. Legros, and I. Monnet, *Nucl. Instr. Meth. B* **268**, 2933 (2010).

<sup>13</sup>G. Sattonnay, S. Moll, L. Thomé, C. Pascanut-Decorse, C. Legros, P. Simon, J. Jagielski, I. Jozwik, and I. Monnet, *J. Appl. Phys.* **108**, 103512 (2010).

<sup>14</sup>J. Zhang, M. Lang, R. C. Ewing, R. Devanathan, W. J. Weber, and M. Toulemonde, *J. Mater. Res.* **25**, 7, 1344 (2010).

<sup>15</sup>Calculations performed with *The Stopping Range of Ions in Matter* J. F. Ziegler, M. D. Ziegler, and J. P. Biersack available on [<http://www.srim.org>].

<sup>16</sup>L. Nowicki, A. Turos, R. Ratajczak, A. Stonert, and F. Garrido, *Nucl. Instr. Meth. B* **240**, 1–2, 277 (2005).

<sup>17</sup>F. X. Zhang, B. Manoun, and S. K. Saxena, *Mater. Lett.* **60**, 2773 (2006).

<sup>18</sup>N. J. Hess, B. D. Begg, S. D. Conradson, D. E. McCready, P. L. Gassman, and W. J. Weber, *J. Phys. Chem. B* **106**, 4663 (2002).

<sup>19</sup>J. F. Gibbons, *Proc. IEEE* **60**, 1062 (1972).

<sup>20</sup>S. Moll, L. Thomé, G. Sattonnay, A. Debelle, F. Garrido, L. Vincent, and J. Jagielski, *J. Appl. Phys.* **106**, 073509 (2009).

<sup>21</sup>W. J. Weber, *Nucl. Instr. Meth. B* **166-167**, 98 (2000).

<sup>22</sup>Y. Zhang, W. J. Weber, W. Jiang, A. Hallen, and G. Possnert, *J. Appl. Phys.* **91**, 6388 (2002).

<sup>23</sup>J. Jagielski and L. Thomé, *Appl. Phys. A* **97**, 1, 147 (2009).

<sup>24</sup>J. Jagielski and L. Thomé, *Radiat. Eff. Defects in Solids* **166**, 367 (2011).

<sup>25</sup>S. U. Campisano, S. Coffa, V. Rainieri, F. Priolo, and E. Rimini, *Nucl. Instr. Meth. B* **80-81**, 514 (1993).

<sup>26</sup>Y. Zhang, W. J. Weber, V. Shutthanandan, R. Devanathan, S. Thevuthasan, G. Balakrishnan, and D. M. Paul, *J. Appl. Phys.* **95**, 5, 2866 (2004).

<sup>27</sup>Y. Zhang, J. Jagielski, I. T. Bae, X. Xiang, L. Thome, G. Balakrishnan, D. M. Paul, and W. J. Weber, *Nucl. Instr. Meth. Phys. Res. B* **268**, 19, 3009 (2010).

<sup>28</sup>Z. Zolnai, A. Ster, N. Q. Khanh, G. Battistig, T. Lohner, J. Gyulai, E. Kotai, and M. Posselt, *J. Appl. Phys.* **101**, 023502 (2007).

<sup>29</sup>A. Debelle, L. Thomé, D. Dompont, A. Boule, F. Garrido, J. Jagielski, and D. Chaussende, *J. Phys. D: Appl. Phys.* **43**, 455408 (2010).

<sup>30</sup>R. Devanathan, W. J. Weber, and J. D. Gale, *Energy and Environmental Science* **3**, 10, 1551 (2010).

<sup>31</sup>F. Gao and W. J. Weber, *J. Appl. Phys.* **89**, 4275 (2001).

<sup>32</sup>F. Gao and W. J. Weber, *Phys. Rev. B* **66**, 024106 (2002).

<sup>33</sup>H. Y. Xiao, F. Gao, and W. J. Weber, *J. Phys. Condens. Matter* **22**, 41, 415801 (2010).

<sup>34</sup>R. E. Williford, W. J. Weber, R. Devanathan, and J. D. Gale, *J. Electroceramics* **3**, 4, 409 (1999).

<sup>35</sup>W. J. Weber and R. C. Ewing, *Radiation Effects in Crystalline Oxide Host Phases for the Immobilization of Actinides*, in *Scientific Basis for Nuclear Waste Management XXV*, edited by B. P. McGrail and G. A. Cragolino (Mater. Res. Soc. Symp. Proc. 713, Warrendale, PA, 2002), p. 443.